Journal of Structural Geology 33 (2011) 1650–1661

Contents lists available at SciVerse ScienceDirect

Journal of Structural Geology

journal homepage: www.elsevier.com/locate/jsg

Displacement–length scaling of brittle faults in ductile shear

Bernhard Grasemann[a,*], Ulrike Exner[a], Cornelius Tschegg[b]

[a] Department for Geodynamics and Sedimentology, University of Vienna, Althanstrasse 14, 1090 Vienna, Austria
[b] Department of Lithospheric Research, University of Vienna, Althanstrasse 14, 1090 Vienna, Austria

ARTICLE INFO

Article history:
Received 18 February 2011
Received in revised form
22 August 2011
Accepted 24 August 2011
Available online 1 September 2011

Keywords:
Displacement–length scaling
Flanking structures
Displacement profiles
Displacement gradient
Triclinic structures
Cyclades

ABSTRACT

Within a low-grade ductile shear zone, we investigated exceptionally well exposed brittle faults, which accumulated antithetic slip and rotated into the shearing direction. The foliation planes of the mylonitic host rock intersect the faults approximately at their centre and exhibit ductile reverse drag. Three types of brittle faults can be distinguished: (i) Faults developing on pre-existing K-feldspar/mica veins that are oblique to the shear direction. These faults have triclinic flanking structures. (ii) Wing cracks opening as mode I fractures at the tips of the triclinic flanking structures, perpendicular to the shear direction. These cracks are reactivated as faults with antithetic shear, extend from the parent K-feldspar/mica veins and form a complex linked flanking structure system. (iii) Joints forming perpendicular to the shearing direction are deformed to form monoclinic flanking structures. Triclinic and monoclinic flanking structures record elliptical displacement–distance profiles with steep displacement gradients at the fault tips by ductile flow in the host rocks, resulting in reverse drag of the foliation planes. These structures record one of the greatest maximum displacement/length ratios reported from natural fault structures. These exceptionally high ratios can be explained by localized antithetic displacement along brittle slip surfaces, which did not propagate during their rotation during surrounding ductile flow.

1. Introduction

Geological faults are shear fractures in rocks that may range in length from less than a centimetre to more than 1000 km, allowing the study of fault evolution, deformation processes and scaling over an exceptionally wide scale range. Field studies of fault displacement profiles and maximum displacement versus fault length are numerous for brittle faults in various rock types with different mechanical properties (e.g. Muraoka and Kamata, 1983; Rippon, 1985; Barnett et al., 1987; Walsh and Watterson, 1988, 1989; Peacock, 1991; Peacock and Sanderson, 1991; Cowie and Scholz, 1992a, 1992b; Gillespie et al., 1992; Dawers et al., 1993; Cartwright et al., 1995; Schlische et al., 1996; Kim and Sanderson, 2005; Soliva and Benedicto, 2005; Schultz et al., 2008; Exner and Grasemann, 2010). Numerical elastic solutions demonstrated that the three-dimensional shape of a brittle fault strongly influences the magnitude of the displacement, and therefore controls the magnitude and spatial distribution of stress in the host rocks (Willemse et al., 1996). The aspect ratio of the fault is defined as the length L (measured as the trace length on a horizontal plane going through the centre of the fault) divided by the fault height H (measured along the fault surface in the dip direction). Keeping L constant, vertically tall faults (smaller aspect ratio) have a greater maximum slip than short faults (greater aspect ratio). For natural blind isolated faults in a layered sequence, the average aspect ratio is about 2 (Nicol et al., 1996). This ellipticity is considered to be the result of either the mechanical heterogeneity of the rock sequence or to the energy difference between screw and edge dislocation (Walsh and Watterson, 1989).

In special cases, an intimate interplay between localized brittle fracturing and more distributed ductile flow is documented, where precursor fractures determine the localisation of ductile shear zones (e.g. Segall and Simpson, 1986; Guermani and Pennacchioni, 1998; Mancktelow and Pennacchioni, 2005; Pennacchioni and Mancktelow, 2007). Distributed ductile deformation and localized slip on discrete fractures can also occur synchronously (Fusseis et al., 2006) or in alternating brittle and ductile episodes (Mancktelow and Pennacchioni, 2005). Flanking structures (e.g. Passchier, 2001; Grasemann and Stüwe, 2001; Exner et al., 2004; Kocher and Mancktelow, 2006), which are the focus of this study, are characterized by distributed deformation of host rock layers around discrete faults. These types of fault-related folds (Schlische, 1995; Withjack et al., 2002) are particularly clear examples of interacting brittle and ductile deformation, because their geometry can only be explained if discrete slip occurred synchronously with the surrounding, distributed ductile flow (Mancktelow, 2008).

* Corresponding author. Fax: +43 (1) 4277 95 34.
E-mail address: Bernhard.Grasemann@univie.ac.at (B. Grasemann).

0191-8141/
doi:10.1016/j.jsg.2011.08.008

Previous numerical, analytical and analogue studies of flanking structures treated the slip surface either as low viscosity inclusion embedded in a higher viscosity matrix or as a brittle fault (e.g. Grasemann and Stüwe, 2001; Grasemann et al., 2003, 2005; Exner et al., 2004; Kocher and Mancktelow, 2006; Exner and Dabrowski, 2010). Many natural examples do not provide clear evidence for the existence of a weak material along the slip surfaces. Thus, even though the kinematics, mechanical interaction and progressive evolution of flanking structures are well constrained, some crucial questions related to the slip along brittle faults deforming in a viscous matrix remained unsolved: 1) What are the different deformation mechanisms within the brittle slip surface with respect to the ductile host shear zone? 2) Because magnitude of the deflection of the host rocks is a direct function of the displacement gradient along the slip surface (Grasemann et al., 2005), what are the shapes of displacement profiles and maximum displacement versus fault length scaling relationships for flanking structures and how do they compare with published data for brittle faults? 3) What is the aspect ratio of brittle faults deforming in a viscous matrix and how does the three-dimensional shape of these faults influence the magnitude of the displacement? 4) What are the displacement profiles of complex flanking structures, which interact or which have a slip surface, which is oriented oblique to the flow direction?

Addressing these questions, we investigate exceptionally well exposed flanking structures from a roughly 1 m thick greenschist facies shear zone on the island of Serifos (Greece). We focus on high-precision measurements of displacement-normal, layer–parallel profiles and present evidences for cataclastic deformation within the slip surface during overall ductile flow.

2. Geological outline

Serifos, located about 100 km SSE of Athens in the Western Cyclades, geologically belongs to the Cycladic Blueschist Unit, which experienced a subduction-related Eocene high-pressure metamorphism followed by Miocene extension and greenschist facies overprint (for a recent review see Jolivet and Brun, 2010; Ring et al., 2010). This Miocene extension occurred in Cordilleran-type metamorphic core complexes (Lister et al., 1984) with detachments showing mainly a top-to-the-N or NE sense of shear (e.g. Buick, 1991; Faure et al., 1991; Gautier et al., 1993; Jolivet et al., 1994, 2010), while in Serifos (Fig. 1), a system of extensional low-angle faults records a clear top-to-the-SSW sense of shear (Grasemann and Petrakakis, 2007; Tschegg and Grasemann, 2009). In addition, the detachment system is syn-kinematically intruded by a Late Miocene high-level I-type granodiorite pluton, with intrusion ages of the main intrusive body and its associated dykes of 11.6–9.5 Ma (Iglseder et al., 2009) followed by rapid cooling (Brichau et al., 2010, and references cited therein). The granodiorite discordantly intrudes a lower detachment, which separates the Cycladic Blueschist Unit from the Cycladic Basement Unit below. Along the southern margin of the granodiorite, the roof is deformed by an upper detachment under ductile to brittle conditions during cooling and exhumation of the rocks (Tschegg and Grasemann, 2009). Where the host rocks of the granodiorite are unaffected by the detachments, older structures are preserved with a dominant ENE-WSW trending lineation probably related to the earlier high-pressure event. In areas where the Miocene low-angle detachments occur, earlier structures are overprinted by a stretching lineation strictly trending NNE-SSW. The structures presented in this paper occur in a mylonitic granitoid in the SE of Serifos, which belong to the Cycladic Basement Unit (black arrow in Fig. 1; see also KML file in supplementary materials).

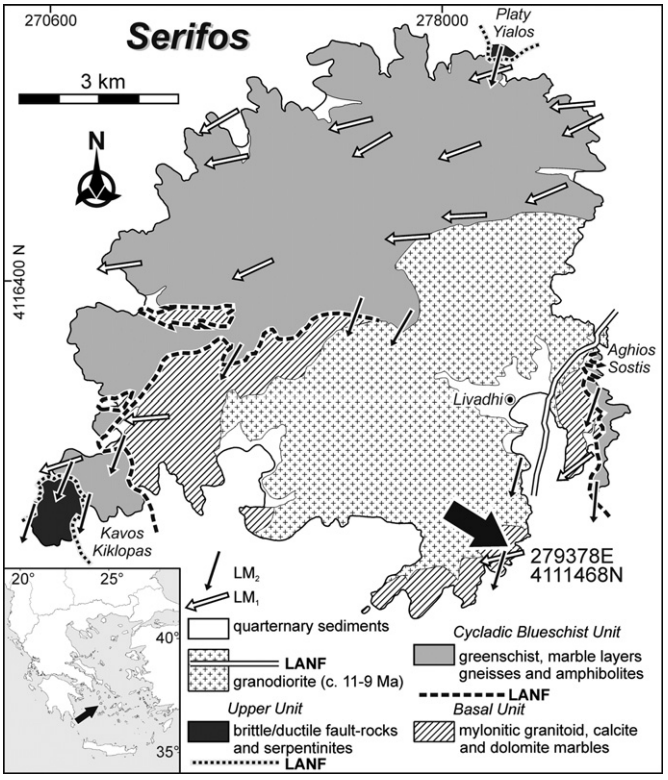

Fig. 1. Geological map of Serifos located in the Western Cyclades in Greece (simplified and modified after Grasemann and Petrakakis, 2007). The investigated outcrop, located in the mylonitic granitoid of the Cycladic Basement Unit, is indicated with an arrow.

3. Monoclinic and triclinic flanking structures

The host of the investigated structures is a mylonitic granitoid rock, which consists mainly of quartz, albitic plagioclase, K-feldspar, muscovite and biotite and has a strong planar, subhorizontal foliation (SM_1) and a stretching lineation LM_1 trending ENE-WSW (Figs. 2 and 3). Throughout this work, subscript 1 represents structures, which are related to a deformation event pre-dating the discordant Late-Miocene intrusive bodies, i.e. the granodiorite and associated dykes. Subscript 2 indicates structural elements that affected the granodiorite and associated dykes and, which are related to the Late Miocene extension event (Fig. 4). After mylonitization, which generated the SM_1 foliation, isolated veins SJ_1 formed locally at a high angle to SM_1 and parallel to LM_1 (Stage 1, Fig. 5). These veins are up to tens of centimetres long and are characterized by a quartz/K-feldspar filling. Muscovite, statically crystallized with the {001} planes parallel to the joints, which either formed along the margins or the centre of the veins (Fig. 6a), and which do not indicate evidences for dynamic recrystallization, kinking or mechanical breaking/fracturing (Fig. 6b).

During the Late Miocene extension, SM_1 was locally reactivated by a greenschist facies mylonitic foliation SM_2 with an NNE-SSW trending lineation LM_2, deviating ca. 30–40° from LM_1 (Stage 2, Fig. 5). These SM_2 shear zones are several metres long and are either parallel to SM_1 or intersect SM_1 at small angles (Fig. 2a). All kinematic indicators (mainly shear bands, quartz fabrics/textures and the flanking structures) indicate top-to-the-SSW shear sense. It is important to note that the outcrop is structurally located in the footwall of the main detachments and records only minor amounts of localized Late Miocene SM_2 deformation and finite strain. Therefore, older structural elements like LM_1 or SJ_1 are preserved outside and at the margins of the SM_2 shear zones (Fig. 2b). A new

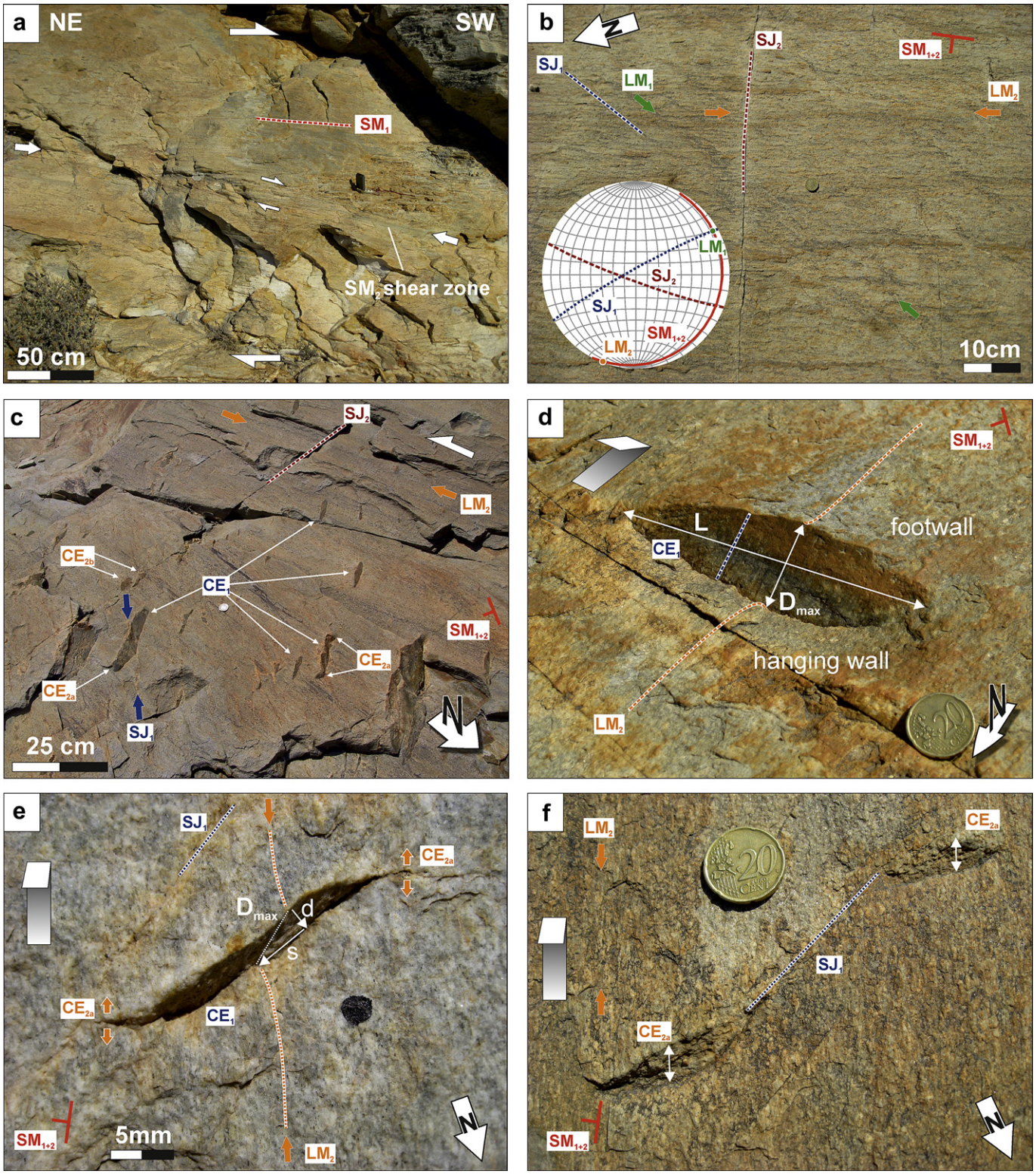

Fig. 2. Field geometries at study sites (see Fig. 4 for illustration of structural labels): a) Localized several meters long SSW-dipping SM_2 shear zone within the mylonitic granitoid, overprinting the earlier SM_1 foliation with an ENE-WSW trending lineation. b) View downward onto the SM_{1+2} foliation plane showing the overprinting of an earlier ENE-WSW (LM_1) by a younger NNE-SSW trending lineation (LM_2). Note, that generally SM_1 is parallel to SM_2, which is indicated by the index SM_{1+2}. c) Several triclinic (CE_1) and some monoclinic (CE_{2b}) flanking structures cutting a single SM_2-foliation plane. Some CE_1 and CE_{2b}-surfaces are connected to linked flanking structures. d) Isolated slip surface of a triclinic flanking structure (CE_1) cutting through the mylonitic foliation plane SM_2. Note the reverse drag of the foliation. e) Triclinic flanking structure with a pronounced strike-slip component (s) with respect to the dip-slip component (d) on CE_1. Due to the strike-slip component, the lineation LM_2 records a reverse drag within the foliation (view downwards onto the foliation). f) Wing cracks CE_{2a}, which were rotated into the shearing direction (view downwards onto the foliation).

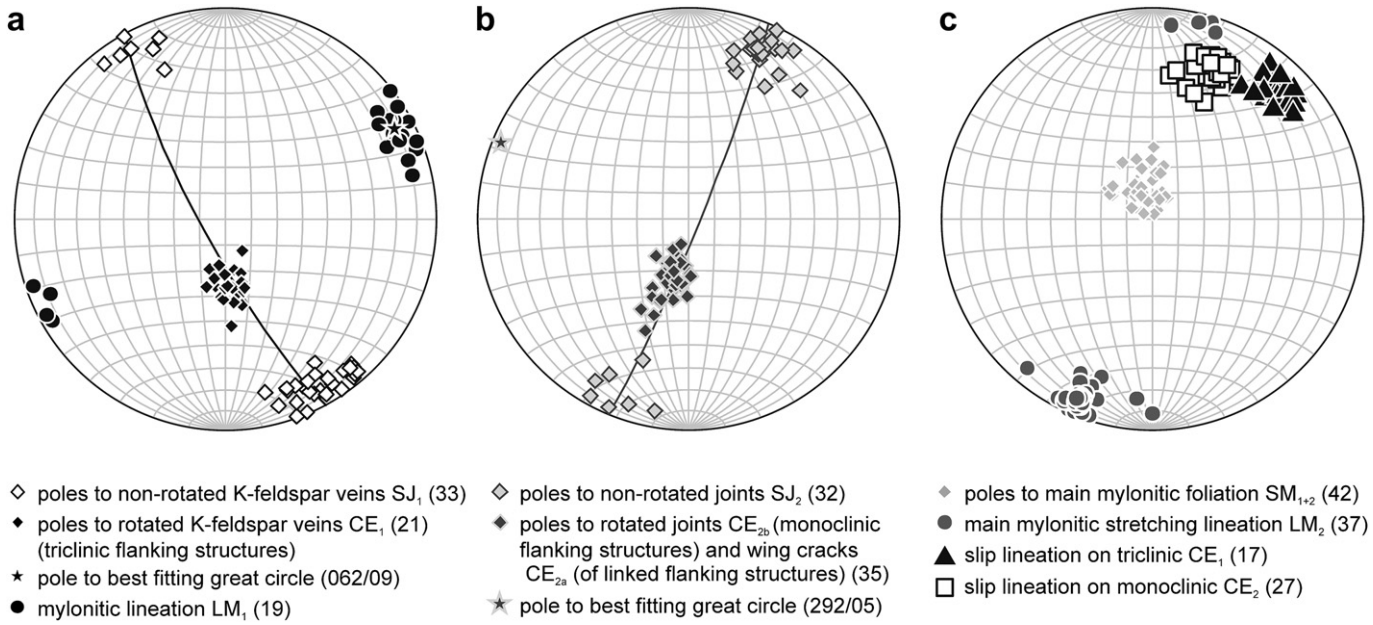

Fig. 3. a) Equal area plots (lower-hemisphere) of non-rotated K-feldspar veins (SJ_1) and ENE-WSW trending lineation LM_1 outside the SM_2 shear zone. Rotated K-feldspar veins CE_1 form triclinic flanking structures. b) Orientations of non-rotated joints (SJ_2) outside SM_2 shear zone. Rotated joints CE_{2b} form monolinic flanking structures; wing cracks CE_{2a} are associated with CE_1 as linked flanking structures. c) Orientations of main foliation SM_{1+2} and lineation LM_2. Note the different orientation of the brittle slickensides on the triclinic (CE_1) and monoclinic (CE_2) flanking structures.

joint system forms perpendicular to LM_2, postdating the formation of SM_2.

In the outcrop, a roughly 1 m thick SM_2 shear zone is exposed for about 2500 m^2 with the center located at 279378E and 4111468N (UTM 35N). The exposed mylonitic foliation surface is roughly in the center of a SM_2 shear zone and dips about 10° towards SE. The foliation is cut by numerous slip surfaces (Fig. 2c), which typically form isolated elliptical planes between the cut-offs of the hanging wall and the footwall (Fig. 2c). The mylonitic foliation can be traced continuously from the footwall to the hanging wall around the tips of the slip surfaces. The slip surfaces exhibit a normal-sense offset with a large displacement gradient along the length of the slip plane and with a maximum offset in the center of the structure. As a result of the large displacement gradient away from the fault plane, the foliation exhibits reverse drag, i.e. the foliation is flexed downward in the hanging wall and upward in the footwall. Therefore, therefore the structures can be classified as flanking structures (Passchier, 2001; Grasemann and Stüwe, 2001). The length L of the exposed slip surfaces varies between 2 and 27 cm and the maximum displacement D_{max} varies between 1 and 11 cm (Fig. 2c, for the measured displacements as a function of position on some of the fractures see the table in the supplementary materials).

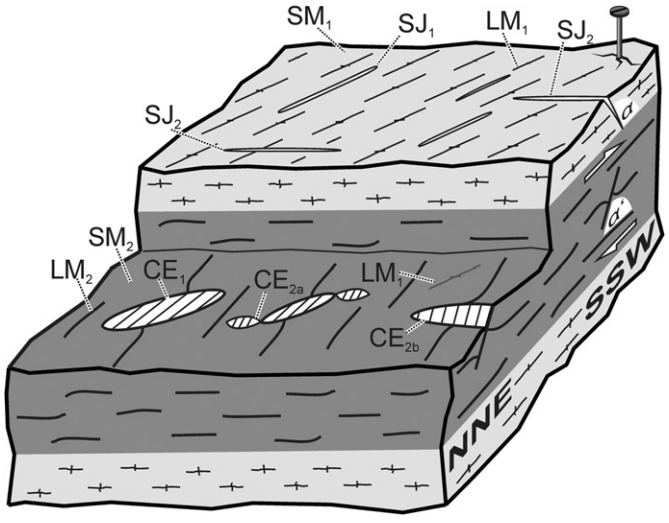

Fig. 4. Synoptic block diagram of the investigated structures. Outside the SM_2 shear zone (indicated in grey): high-grade mylonitic SM_1 foliation with associated LM_1 stretching lineation; K-feldspar veins (SJ_1); joints (SJ_2). Inside the SM_2 shear zone: low-grade mylonitic SM_2 foliation with associated LM_2 stretching lineation overprints remnants of LM_1 lineations; rotated SJ_1 K-feldspar veins form triclinic flanking structures CE_1. Rotated SJ_2 joints form monolinic flanking structures CE_{2b}; and wing cracks CE_{2a} are associated with CE_1 as linked flanking structures. The orientation α of SJ_2 with respect to SM1 and the orientation α' of CE_{2b} can be used to calculate the shear strain of the SM_2 shear zone.

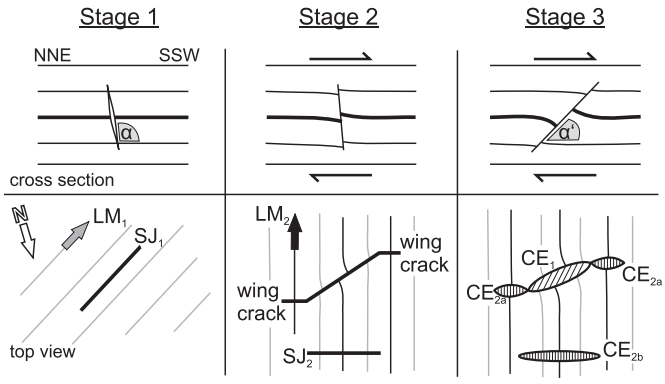

Fig. 5. Deformation sequence for the investigated structures. The top row shows a cross section in the xz plane parallel to LM_2. The bottom row shows a top view. During Stage 1, SJ_1 K-feldspar veins developed parallel to the mylonitic lineation LM_1. During Stage 2, a new lineation LM_2 formed as a result of SSW-directed shearing. Joints SJ_2 and wing cracks developed perpendicular to the LM_2. During Stage 3 all discontinuities rotated during SSW-directed shearing forming triclinic (CE_1) and monoclinic (CE_{2b}) flanking structures. Wing cracks CE_{2a} and CE_1 formed linked flanking structures. Orientations of SJ_2 before (α) and after (α') shearing.

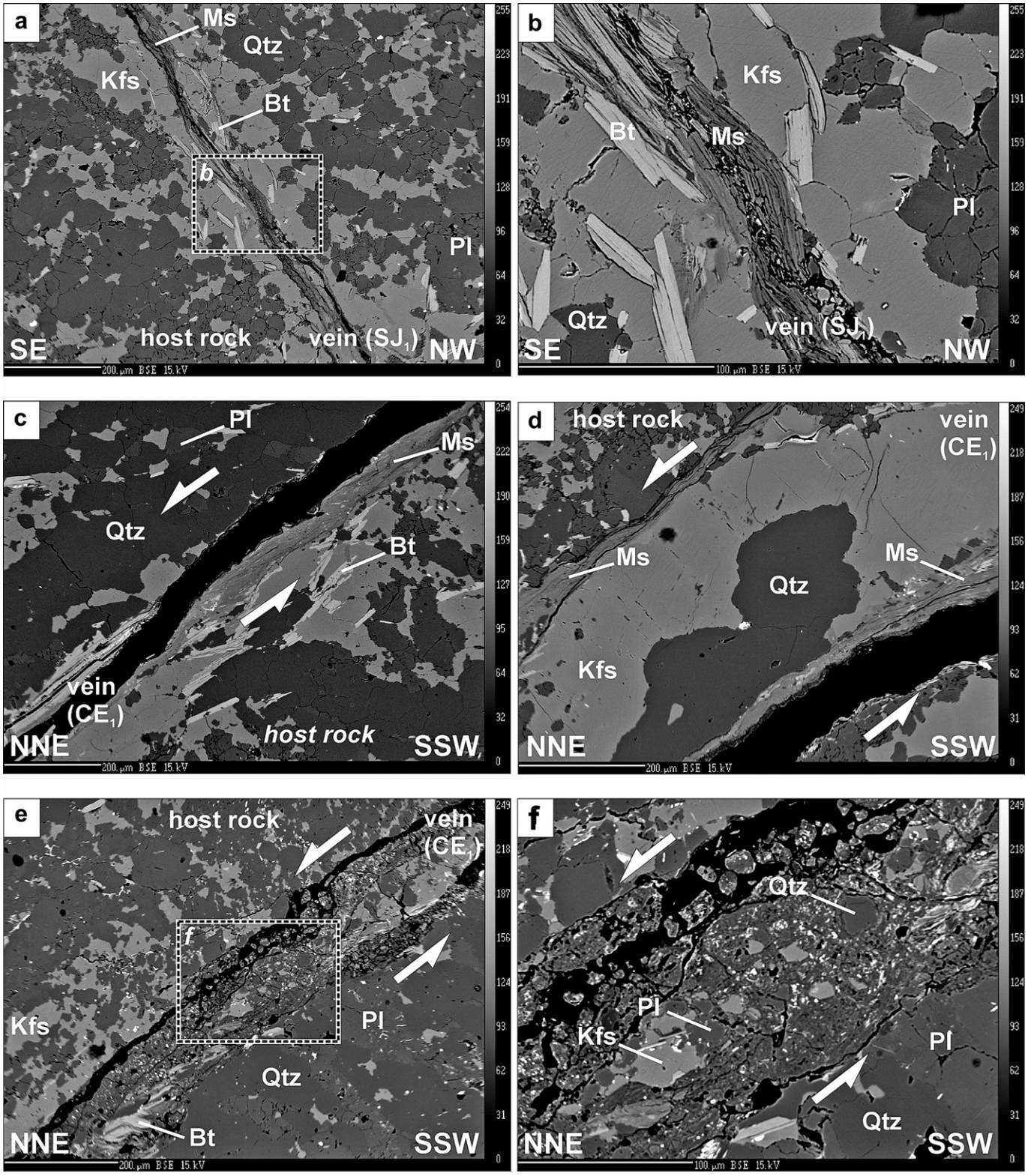

Fig. 6. Electron microprobe backscattered electron images of veins (a and b, sample SN1/09, 279383E, 4111484N) and cross-cutting elements of the flanking structures (c and d, sample 207/SE1, 279423E, 4111466N). a) K-feldspar/quartz vein with crystallized muscovite layer. The host wall rocks consist of albitic plagioclase, K-feldspar, quartz, and biotite grains. b) Detail of Fig. 6a showing statically muscovite blastesis along a joint within or at the margin of the K-feldspar vein. c) Reactivated joint with localization of deformation in the muscovite forming top to the NNE SC'-fabrics. d) Reactivated K-feldspar/quartz vein, again showing localization of slip along muscovite layers between vein and host rock. e) Cataclastically deforming K-feldspar/quartz vein. f) Detail of Fig. 6e. All analyses were performed on a Cameca SX-100 electron microprobe (Department of Lithospheric Research, University of Vienna) according to the method and measurement conditions described in Tschegg and Grasemann (2009).

The flanking structures developed by localization of deformation on pre-existing joints or veins (e.g. Segall and Simpson, 1986; Mancktelow and Pennacchioni, 2005), which originally had a large angle to the foliation and rotated during SSW-directed ductile flow into the shearing direction. During rotation the slip surfaces recorded an antithetic shear with respect to the SSW-directed flow (Stage 3, Fig. 5) and two-dimensional sections through the center of the structures show a-type flanking structures (Grasemann et al., 2003). These structures are particularly clear examples of interacting localized and distributed deformation because their geometry is best explained as discrete slip on the faults synchronous with distributed ductile flow in the host rocks (Mancktelow, 2008). In detail, the slip surfaces of the flanking structures developed on three different types of discontinuities, which are referred to as cross-cutting elements (CE) throughout this study:

(i) The veins and joint generation SJ_1 was reactivated as cross-cutting elements CE_1 (Fig. 2e), which represent about 80% of the flanking structures in the outcrop. The slip on CE_1 is documented by mechanical grain-size reduction and breakup of the muscovite minerals present in the quartz and K-feldspar rich veins. The resulting 50 μm thick layer of fine-grained mica flakes shows a sc-type internal fabric (Fig. 6c and d), indicating slip accommodation. In parts of the veins, where these muscovite layers are scarce or totally missing, the vein filling (mainly quartz and K-feldspar rich material) was deformed by cataclastic crushing and rotation of fragments (Fig. 6e and f). This difference is most striking, comparing Fig. 6d, in which the vein is still intact due to presence of muscovite layers to Fig. 6e in which the vein is cataclastically completely disintegrated and lacks any muscovite. This observation suggests that the deformation within the CE of the flanking structures occurred by frictional deformation mechanisms while the slip surface rotated within the shear zone and developed drag of the mylonitic foliation by ductile flow (compare Fig. 2d). The original orientation of SJ_1 is oblique to the flow direction, thus the resolved slip on CE_1 records a dip and a strike-slip component. As both the dip-slip and the strike-slip component display a displacement gradient (Fig. 2e), fault drag is visible in the dip direction (visible in a drag of the foliation SM_{1+2}) but also in the strike direction of CE_1 (visible in a drag of LM_2 within SM_{1+2}). The overall flanking structure has a triclinic symmetry and therefore the structures developed along CE_1 are *triclinic flanking structures* (compare Fig. 5, Stage 3).

(ii) Some of the investigated CE_1 surfaces have either curved tips (Fig. 2d and e) or younger secondary fractures CE_{2a} at the tips of rotated SJ_1 surfaces (Fig. 2f). The shape of these secondary fractures clearly resemble wing cracks, which are frequently observed in uniaxial compression experiments of brittle materials containing a pre-existing crack (e.g Mutlu and Pollard, 2008; Wang and Mora, 2008 and references cited therein). Wing cracks are mode I (tensile) fractures, that nucleate at the tips of mode II or III (shear) fractures (Brace and Bombolakis, 1963). Although fundamental mechanical differences exist between models for wing cracks and our flanking structures, the structures have in common that a pre-existing SJ_1 is reactivated as a shearing-mode slip-surface CE_1 and that the initial CE_{2a} forms analogously to mode I fractures in the form of wing cracks. During ongoing SSW-directed shear, CE_{2a} is reactivated as a slip surface and rotates into the shear direction (Fig. 2f). CE_{2a} forms almost perpendicular to the flow direction, thus the offset along the flanking structure records a dominant dip-slip component with normal drag of the main foliation. The complex structures, which have a triclinic symmetry and developed along the linked cross-cutting elements CE_1 and CE_{2a} are *linked flanking structures.*

(iii) At a late stage of the Late Miocene extension, SJ_2 joints form perpendicular to the LM_2 lineation. These joints also pervasively cut the granodiorite intrusion. Some SJ_2 joints were affected by ductile shearing, and form CE_{2b} slip surfaces with pure dip-slip offset and associated flanking structures with a monoclinic symmetry (Fig. 2c). The deformation along CE_{2b} is also brittle forming slickensides with slickenlines. The structures developed along CE_{2b} are *monoclinic flanking structures.*

3.1. Displacement–distance measurements

The flanking structures in the outcrop have the advantage of being extremely well exposed, a large number present in a small area, all confined to the same lithology, and some examples that can even be studied on two different sections (parallel and perpendicular to the mylonitic foliation). Using a micro-ruler, the displacement profiles were directly measured in the outcrop as displacement D along the lineation on the slip surface and distance X from midpoint to the center of the slip surface. Only isolated slip surfaces associated with smooth deflection of the surrounding mylonitic foliation that could be traced continuously from the footwall around the lateral tips to the hanging wall were included in the measurements (e.g. Fig. 2d). Measurement errors due to uneven erosion of the mylonitic foliation and the slip plane are about ±1 mm (the complete dataset is listed in Table 1, supplementary materials). The measured elliptical slip surface (e.g. in Fig. 2d) does not represent the full size of the CE surface of the flanking structure, but only the part which is exposed between the cut-off of the exposed mylonitic foliation on the footwall and hanging wall. Fig. 7 shows the normalized displacement–distance plots (i.e. offset D versus position X along the trace of the slip surface) of 12 triclinic, 8 monoclinic and 4 linked flanking structures. All position measurements, X, have the origin of the coordinate system in the center of the flanking structure. The offset and the position were normalized by the half length $a = L/2$ of the slip surface (L is the total strike length of the slip surface).

The majority of the measured data of monoclinic and triclinic flanking structures record a maximum displacement in the center of the slip surface with a symmetric decrease of the displacement towards the tips. Few flanking structures (e.g. FF14, FF5, FF10, FF18 in Fig. 7a and b) record a slightly asymmetric slip distribution. The linked flanking structures clearly deviate from such ideal displacement profiles, as they record two displacement maxima in the central segment CE_1 with a local minimum between the two maxima (Fig. 7c). We exclusively observed two maxima on linked flanking structures, usually occurring within CE_1. Obviously the two maxima are related to the development of CE_{2a}. On the structure FF2 (Fig. 7c), a CE_{2a} is only developed on one side of the CE_1 surface; accordingly, this linked flanking structure records only one maximum.

To compare the displacement–distance plots of the triclinic and monoclinic flanking structures, all measured profiles were plotted in a generic plot of dimensionless displacement versus dimensionless distance (Fig. 8a). Because of the more complex displacement profiles, linked flanking structures are not included in this plot. For comparison, the normalized displacement calculated from Eq. (1) is added to the plot (dashed line, Fig. 8a). Note that the scatter of the natural data reflects measurements errors and/or mechanical differences between the model and the natural process forming the flanking structures.

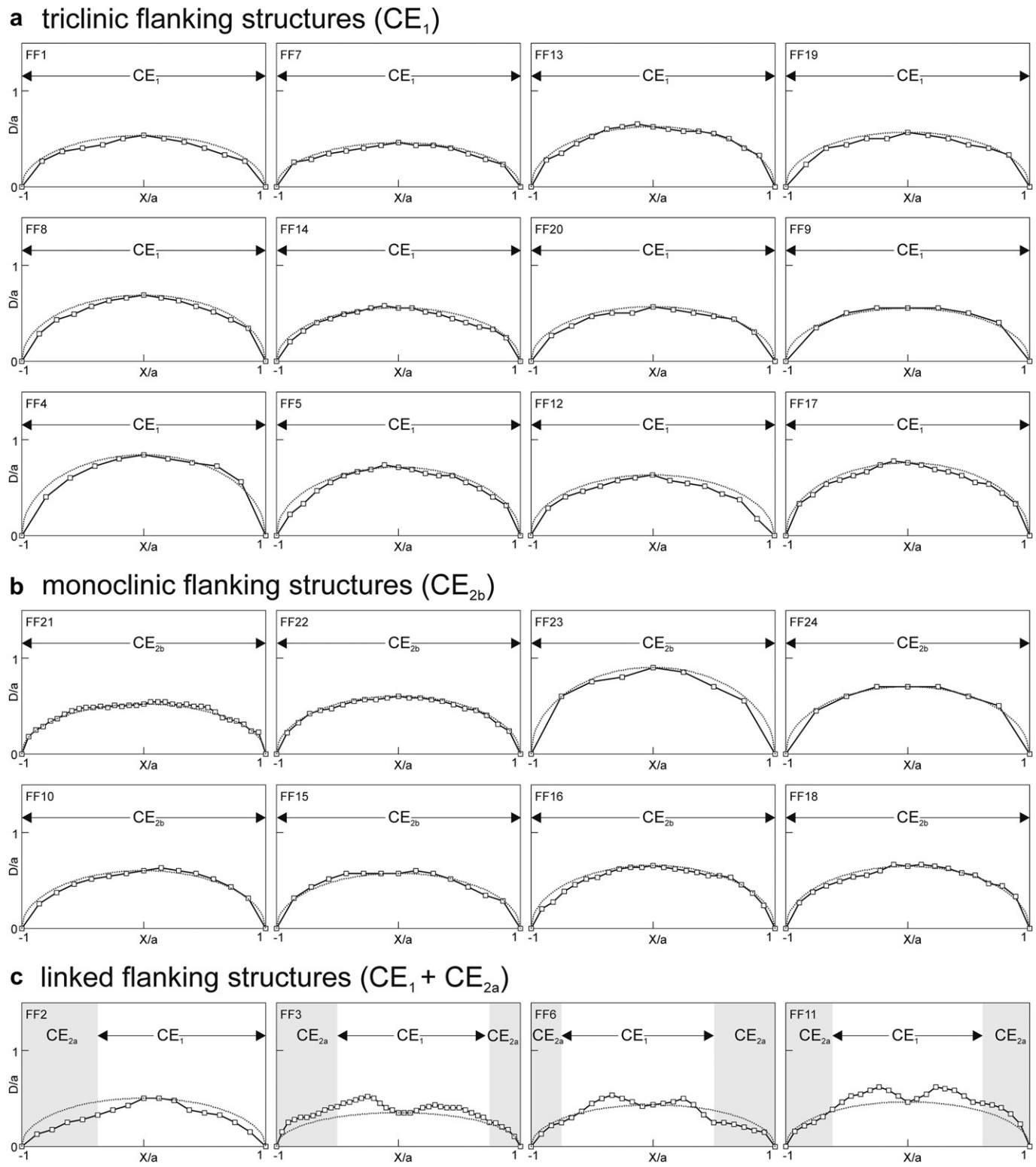

Fig. 7. Normalized displacement (D/a) versus normalized distance (X/a) profiles of a) triclinic CE_1, b) monoclinic CE_{2b} and c) linked flanking CE_1+CE_{2a} structures (shaded parts indicate locations of CE_{2a}). Dotted curve represents the elastic solution for cracks subjected to uniform loads (Eq. (1); Pollard and Segall, 1987).

The measured field data are compared with an elastic solution for cracks subjected to uniform loads (Pollard and Segall, 1987):

$$\frac{D}{a} = 2\Delta\sigma\frac{1-\nu}{G}\sqrt{1-\frac{x^2}{a^2}} \qquad (1)$$

where $\Delta\sigma$ is the shear stress drop, ν is the Poisson's ratio and G the shear modulus. The displacement is greatest at the center of the slip surface and decreases towards the tips to zero where $X = \pm a$. Values for the unknown term $2\Delta\sigma(1-\nu)/G$ are calculated by inserting a and D at $X = 0$ from the measured structure into Eq. (1). The measured displacement–distance profiles are in good agreement with the

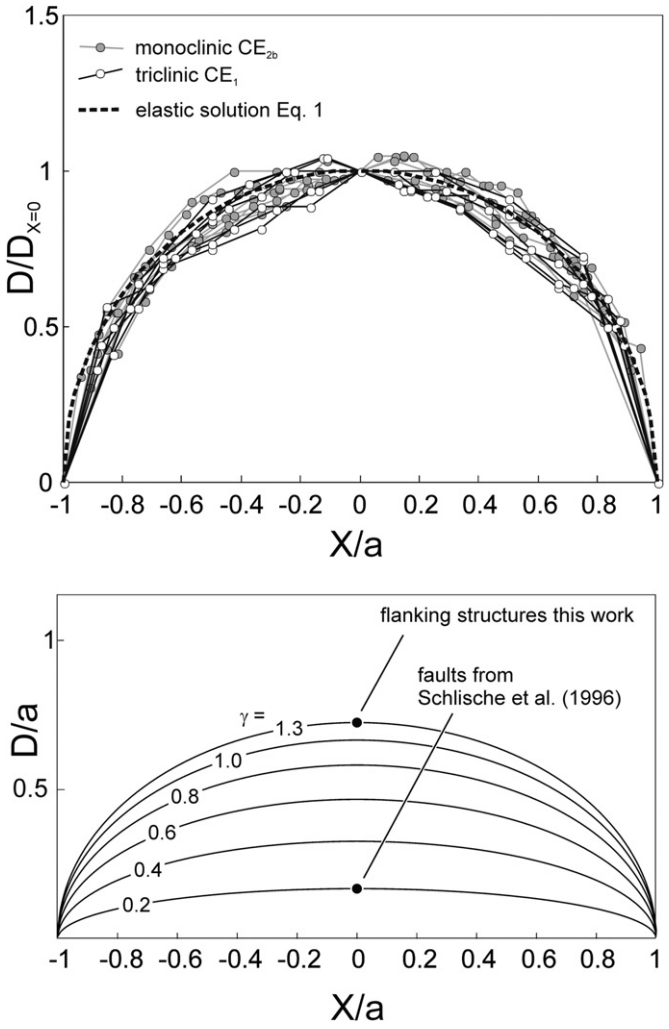

Fig. 8. a) Normalized displacement versus normalized distance profiles of triclinic CE_1 (white dots) and monoclinic CE_{2b} flanking structures (grey dots). Black dashed curve represents the elastic solution for cracks subjected to uniform loads (Eq. (1); Pollard and Segall, 1987). b) Evolution of normalized displacement vs. distance with γ of a synthetic monoclinic flanking structure (using the model of Exner and Dabrowski, 2010) with increasing shear strain γ, from an initially circular CE oriented at 90° to the shear plane. Note that for this initial orientation, the model predicts that the sense of shear is reversed at $\gamma = 1.3$. According to the measured displacement maxima the investigated structures indicate a γ close 1.3.

normalized elastic solutions of Eq. (1) (dotted curves in Fig. 7). The investigated isolated triclinic and monoclinic flanking structures formed by frictional slip but within ductile deforming host rocks and therefore the measured field data are additionally compared with a modified three-dimensional Eshelby solution for a viscous fluid modeling shearing of an elliptical crack oriented perpendicular to the flow direction (for derivations of relevant equations see Exner and Dabrowski, 2010). Fig. 8b shows normalized displacement–length plots of an initially circular CE subjected to simple shear, using the model of Exner and Dabrowski (2010). The initial conditions are chosen to correspond to the monoclinic flanking structures (CE_{2b}) developing from SJ_2 surfaces. All progressive displacement profiles show an elliptical shape, although at small γ, the profiles are more flat than those at larger γ. It is important to note that after $\gamma = 1.3$, the sense of shear is reversed on the CE and the displacement decreased similarly to the previous increase, finally resulting in a contractional offset on the CE (Exner et al., 2004). This model value indicates approximately an upper limit to the maximum finite deformation for the natural examples, because the natural structures do not record a reversal of shear sense or even contractional offset.

3.2. Maximum displacement versus length of the slip surface

Empirical and fracture mechanics models of single isolated faults predict simple power–law relationships between fault length L and maximum slip distance D_{max}:

$$D_{max} = cL^n \quad (2)$$

where c is a constant related to rock properties (Young's modulus, Poisson's ratio) and driving stress and n is the power-law exponent, which lies usually between 1 and 2 (Walsh and Watterson, 1988; Marrett and Allmendinger, 1991; Gillespie et al., 1992; Schultz and Fossen, 2002). Although the investigated structures developed under very different conditions than most faults in published datasets, it is tempting to investigate the D_{max}/L scaling of the measured structures. The length L of the investigated flanking structures (CE_1 and CE_2) span only about one order of magnitude, which normally is too small to fit with an exponent n in a logarithmic plot considering the scatter of published data (Cowie and Scholz, 1992a). However, since the excellent exposure of the structures allowed very accurate measurements reducing data scatter (compare dataset listed in Table 1, supplementary materials), we calculated a best-fit power trendline for the flanking structures with $c = 0.24$ and $n = 0.9$, which is nearly linear (Fig. 9). The coefficient of determination is $R^2 = 0.9$. Comparison with published data of offset measurements along small scale faults (in the range of 1 cm–10 m) highlights the exceptionally large displacement gradient for our flanking structures. The host rocks of all referenced faults (Muraoka and Kamata, 1983; Peacock, 1991; Peacock and Sanderson, 1991; McGrath, 1992; Schlische et al., 1996) are sandstones/siltstones recording normal offset with the

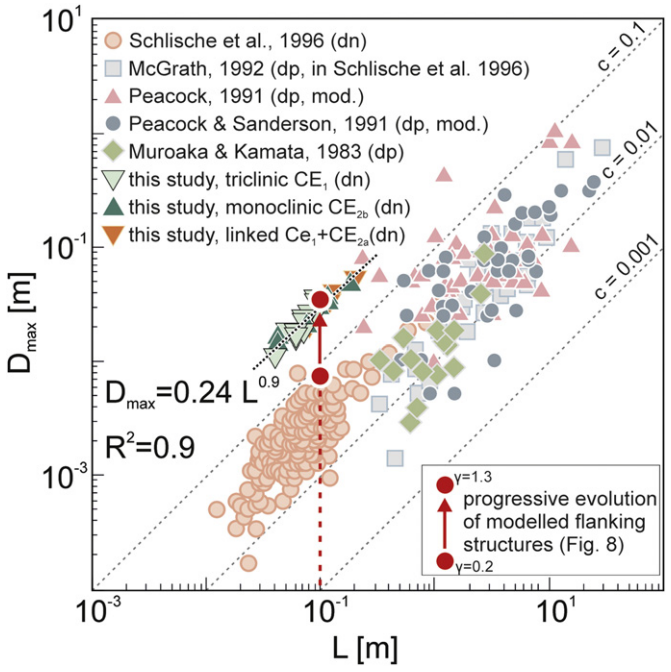

Fig. 9. D_{max}/L scaling of the studied isolated triclinic and monoclinic flanking structures (green triangle) and linked flanking structure (orange triangle). For comparison to our data, data are plotted from published small-scale faults (dn - displacement normal; dp - displacement-parallel). The range of D_{max}/L values for the experiment presented in Fig. 8b are plotted as a red arrow, showing the evolution of D_{max} with increasing γ.

exception of Peacock (1991), who investigated strike-slip faults. Large faults (>several 10 m in length) are not considered in this comparison. Note that only Schlische et al. (1996) and Wibberley et al. (1999) measured displacement-normal, layer–parallel profiles directly comparable to our data. The other referenced measurements were collected along profiles which are parallel to the displacement and normal to the layering and therefore tend to have lower D_{max}/L ratios than displacement-normal, layer–parallel profiles (Peacock, 1991). The original data set of Peacock (1991) and Peacock and Sanderson (1991) define the fault length as the distance between the point of maximum displacement and the fault tip. To compare these data with the other measurements, the maximum displacement was plotted versus the full length of the faults, assuming that the maximum displacement is close to the fault center.

4. Discussion

4.1. Deformation mechanism in the CE of the flanking structures

Formation of the 100–200 μm thick SJ_1 quartz/K-feldspar veins was followed by partial reactivation that formed the flanking structures, and then, a fluid pulse which yielded blastesis of statically growing muscovite minerals along joints. The joints formed either parallel to the vein-host rock contacts or along the center of the veins. Experiencing no further slip, these joints were preserved in this state and are observed outside the shear zone (Fig. 6a and b).

An interesting exercise is to compare the shear strain due to the flanking structures to the shear strain within the brittle fault zones. Considering the flanking structures, the rotation of a passive marker line deforming under simple shear is given by (Ramsay and Huber, 1983):

$$\cot \alpha' = \cot \alpha - \gamma \quad (3)$$

where α is the orientation of a passive marker line before and α' after simple shear deformation for a shear strain γ. Because an elliptical slip-surface subjected to homogeneous shear exhibits the same rotation and stretching as a passive material ellipse with identical aspect ratio (Exner and Dabrowski, 2010), the orientation of the joints SJ_2 outside the shearzone (α) and the orientation of the slip surface of the monoclinic flanking structures within the shearzone (α') can be used to estimate the shear strain γ of the SM_2 shear zone (Fig. 4). The mean dip of SJ_2 is roughly vertical and the monoclinic flanking structures have a cross-cutting element CE_2, which dips with about 30° NNE (Fig. 3). Assuming bulk simple shear during ductile deformation of the SM_2 shear zone and subtracting the 10° dip of the main foliation, the calculated shear strain is $\gamma = 1.37$ ($\alpha = 100°$, $\alpha' = 40°$).

The shear strain within the fault zones themselves can be calculated by dividing the offset of the marker foliation by the thickness of the material within the CE_1. The thickness of the zone of cataclastic deformation within the CE_1 is about 100–200 μm (Fig. 6). The mean offset of the marker foliation of all measured structures is about 2.5 cm (Table 1, supplementary materials), resulting in an average shear strain of $\gamma = 125$-250. Since this offset is a result of the antithetic catclastic slip on the CE_1 during SSW-directed ductile deformation (i.e. shear strain accumulated within the same time span), the strain rate within the slip surface is two orders of magnitude greater than the ductile flow in the host rock. Similar differences between the shear strain rates within the CE and the host rock exist in physical and numerical modelling of flanking structures (Grasemann and Stüwe, 2001; Exner et al., 2004). We suggest that this difference in strain rates within the CE of the flanking structures and in the host rock together with the different texture of the muscovites in the CE are the main cause of synchronous cataclastic deformation in the CE and ductile flow in the host rock.

4.2. Accumulation of displacement along the CE of the flanking structures

Both the isolated monoclinic and triclinic flanking structures have remarkably simple elliptical displacement profiles with a maximum in the center of the slip surface decreasing laterally towards the tips. The structures also record the maximum displacement gradient at the tip of the slip surfaces (see also Gupta and Scholz, 1998). In linear elastic fracture models, abrupt terminations produce infinitely high stresses in the surrounding material around the fault tip, which is clearly unrealistic because real materials have finite strength (Pollard and Segall, 1987). A model more appropriate for the flanking structures is the Eshelby solution modified for a viscous fluid (Exner and Dabrowski, 2010). In this model, the slip surface undergoes homogeneous deformation that stretches and rotates the slip surface while preserving elliptical shape. Monoclinic flanking structures develop if the strike of the slip surface is parallel to the fixed vorticity axis of the homogeneous far field flow. The slip surface shows an elliptical displacement profile in a section along the strike through the center of the structure. An oblique initial orientation of the CE results in a reorientation of the principal axes of the elliptical slip surface during deformation. This effect influences the amount and sense of offset because the resolved shear vector has a component parallel to the vorticity axis of the homogeneous far field flow that introduces an additional non-plane strain deflection of markers. This effect can be clearly seen in the flanking structures because the central mylonitic marker planes record a deflection and the stretching lineation is deflected within the mylonitic foliation across the CE (compare Fig. 2d and e). It is important to note that the analytical models of Exner and Dabrowski (2010) do not allow for a propagation of the slip surface, only a passive rotation and stretching. Such deformation behavior can explain the accumulation of large displacement at constant fault length. Comparing the modeling results (Fig. 8b) with the natural data, we are convinced that this fundamental property of inhibited fault propagation applies for the observed structures, and is moreover a general feature of flanking structures.

4.3. Maximum displacement–length scaling of the flanking structures

Fault maximum displacement–length relations (D_{max}–L) have been a topic of controversial discussions that have mainly focused on the understanding of parameters controlling the scaling laws (e.g. Walsh and Watterson, 1988; Cowie and Scholz, 1992a; Dawers et al., 1993; Schlische et al., 1996; Clark and Cox, 1996; Scholz, 2002; Schultz et al., 2006, 2008). These relations are fundamental because they record the growth history of fault systems (for a review see Kim and Sanderson, 2005). However, the relationship between L and D_{max} of flanking structures is largely unknown. On the other hand, the interpretation of the relationship between L and D_{max} is complicated by the fact that fault-growth models indicate that the scaling relationship should depend on rock properties, thus correlations using data sets combined from different mechanical and rheological conditions may be questionable (Cowie and Scholz, 1992b). Additionally, each data set typically spans only a limited range of fault sizes of about an order of magnitude. This range is too small to fit with an exponent in a log–log plot of D_{max} versus L and requires the scatter to be much less than a factor two or three to be fit reliably in a linear plot, which is a requirement not commonly met by the data (Cowie and

Scholz, 1992b). Despite of these limitations, a unit slope in the D_{max}/L diagram, which implies proportional growth (L/H = const.) has been demonstrated in several data sets (e.g. Schlische et al., 1996 and references cited therein). However, faults may also scale non-proportionally, for example, faults that grow by segment linkage either horizontally or vertically (Peacock, 1991; Cartwright et al., 1995). Laterally restricted faults tend to have greater D_{max}/L ratios than vertically restricted faults (Nicol et al., 1996; Schultz and Fossen, 2002). In general, fractures confined to stratigraphic layers grow non-proportionally, leading to a reduced capacity to accommodate displacement and a shallower slope on a D_{max}/L diagram (Fossen and Hesthammer, 1997; Soliva and Benedicto, 2005; Soliva et al., 2006). Other models explaining non-linear fault growth have been suggested for geologic structural discontinuities that accommodate significant volumetric changes, such as opening (joints, veins, dikes) or closing (compactional shear deformation bands, compaction bands) strains across them (Schultz et al., 2008).

Beside predictions by different mechanical models for fault growth, several authors emphasized the problems associated with measuring D_{max}/L data. Frequently the measured discontinuities are not fully exposed in three dimensions and it is therefore not always clear if the displacement profiles sample the greatest displacement (Muraoka and Kamata, 1983; Walsh and Watterson, 1988; Cowie and Scholz, 1992b; Gillespie et al., 1992; Kim and Sanderson, 2005). Depending on the exposure, some studies collected data parallel to the displacement directions, whereas others measure the displacement gradient perpendicular to this direction. In fact, displacement-parallel and bedding-normal profiles tend to have greater D_{max}/L ratios than displacement-normal, bedding-parallel profiles (Peacock, 1991).

Despite the problems associated with data collection, we compare our data with published D_{max}/L data from other small scale discontinuities (Fig. 9). Most published data for normal faults are from unmetamorphosed sediments and therefore their mechanical formation and rheology differ significantly from that for the flanking structures, which formed in low-grade metamorphic shear zones. Only the dataset of Schlische et al. (1996) shows visible reverse drag adjacent to the isolated slip surfaces and shares many similarities with our structures (Fig. 9), especially the continuous structures in the host rocks and the analogous reverse drag of the bedding planes near the center of the structures. In fact, these structures are comparable to a-type reverse flanking structures (Passchier, 2001; Grasemann et al., 2003), and hence, similar to the structures in this work.

Our D_{max}/L data show an exceptionally good fit of a nearly linear power-law trendline ($n = 0.9$, $R^2 = 0.9$, Fig. 9). The good fit is best explained by the excellent exposure of the structures, which allowed very accurate measurements. The linear relationship can be explained by two different models: (i) All structures formed at the same time and experienced the same amount of far field shear strain. Since the CEs cannot propagate in the viscous host rocks and accommodate deformation by stretching, rotation and antithetic shearing (Exner and Dabrowski, 2010), L remains constant during deformation, accumulating displacement proportional to the size of CE (compare path of modeled flanking structure in Fig. 9). (ii) The CEs are of rather constant size and orientation but their positions are arranged randomly with respect to the exposure surface. In this case, the cut-effect means that most faults are intersected at a distance from the median plane and only apparently have shorter lengths and smaller displacements. Although geologically feasible, this model can be ruled out for the investigated outcrop, because field observations on xz-sections indicate that the size of the CEs range over one order of magnitude and are roughly cut through their center by the exposed xy-section.

To our knowledge, our data have greatest published D_{max}/L ratio of 0.24, which is up to one order of magnitude greater than the mean of all other published data. This large D_{max}/L ratio can be explained by three-dimensional mechanical models of flanking structures developing in viscous flow, which predict stretching of the slip surface into the shear direction (Exner and Dabrowski, 2010.). For the models, which offset of a central marker along an initially circular slip surface deforming by a shear strain of $\gamma = 0.2$ and 1.3 (Fig. 8b), the resulting D_{max}/L ratio ranges between 0.075 and 0.35 (red circles in Fig. 9). The structures from Serifos ($\gamma \sim 1.5$) fit perfectly to the model results calculated for $\gamma = 1.3$. Furthermore, the large D_{max}/L ratio and the associated reverse drag of the mylonitic foliation supports the conclusion of Exner and Grasemann (2010) that discontinuities with a D_{max}/L ratio greater than about 0.01 display a perceptible fault drag, whereas below that value the displacement gradient is insufficient to develop a visible deflection and thus fault drag is not observed.

4.4. Triclinic flanking structures

Theoretical considerations about the variability of triclinic flow types and their likelihood in natural shear zones have been discussed by several authors (e.g., Jiang and Williams, 1998; Lin et al., 1998; Iacopini et al., 2007). In field studies, triclinic transpression zones were identified by the variation in strain geometry and kinematics of differently oriented and kinematically related shear zones or different segments of a curved shear zone (e.g. Lin and Jiang, 2001; Sullivan and Law, 2007). Our shear zone has parallel shear zone boundaries at the outcrop scale and even more importantly, the lineations related to this Miocene extension on the whole island of Serifos are striking consistently NNE-SSW (Grasemann and Petrakakis, 2007). We therefore believe that the flanking structures developed during monoclinic SSW-directed non-coaxial flow.

Nevertheless, the flanking structures, which reactivated the pre-existing vein and joint generation SJ_1 clearly record a triclinic symmetry because the oblique orientation of SJ_1 to the flow direction resulted in dip- and a strike-slip components on CE_1. Three-dimensional analytical solutions demonstrate that shearing along an elliptical cracks oriented oblique to the principal directions of a monoclinic flow result in stretching and rotation of the slip surface preserving an elliptical shape. These flanking structures produce a triclinic symmetry, without necessarily implying triclinic background flow kinematics (Exner and Dabrowski, 2010). Furthermore, the additional occurrence of monoclinic flanking structures in this outcrop, which can be unequivocally attributed to a different set of pre-existing joints, supports this assumption of a monoclinic flow in the shear zone.

5. Conclusions

1) This study investigates discontinuities (veins and joints), which form flanking structures by accumulating antithetic brittle slip and rotating in a ductile shear zone into the shear direction. Depending on the initial orientation of the discontinuity, either triclinic, monoclinic or linked flanking structures with wing cracks developed.
2) The structures, which developed ductile drag of foliation in the host rocks during cataclastic deformation of K-feldspar, quartz and muscovite within the slip surface of the flanking structure, are examples of synchronous brittle and ductile deformation. Brittle deformation may be triggered by strain rates within the slip surface which are two orders of magnitude greater than the strain rates in the host rock.
3) The displacement variations along the strike length of both the triclinic and the monoclinic flanking structures record nearly

ideal elliptical profiles. The large displacement gradients are accommodated by ductile flow in the host rock through reverse drag of the foliation planes crossing the centre of the faults.

4) The maximum displacement versus fault size data of flanking structures have, to our knowledge, the greatest published D_{max}/L ratio of 0.24, which can be explained by rotation and localized antithetic displacement of a non-propagating slip surface rotating in a ductile shear zone with low finite shear strain.
5) The high D_{max}/L ratios support the prediction that discontinuities with a D_{max}/L ratio higher than about 0.01 display a perceptible fault drag.

Acknowledgement

This work has been supported by the FWF Austrian Science Fund (P18823-N19, P18908-N19 and T325-N14). Christian Rambousek discovered the studied outcrop during field work for his master thesis. Fruitful discussions with Marcin Dabrowski, Marcel Frehner, Neil Mancktelow, Steve Martel, Hugh Rice, and Gerhard Wiesmayr are gratefully acknowledged. S. Hrabe, C. Beybel and L. Slawek are thanked for high-quality thin section preparation. We thank Roy Schlische and an anonymous referee for important comments on our manuscript, which improved both content and style. Detailed editorial and scientific comments of the editor Bill Dunne are gratefully acknowledged.

Appendix. Supplementary material

Supplementary material associated with this article can be found, in the online version, at doi:10.1016/j.jsg.2011.08.008.

References

Barnett, J.A.M., Mortimer, J., Rippon, J.H., Walsh, J.J., Watterson, J., 1987. Displacement geometry in the volume containing a single normal fault. The American Association of Petroleum Geologist Bulletin 71, 925–937.
Brace, W.F., Bombolakis, E.G., 1963. A note on brittle crack growth in compression. Journal of Geophysical Research 68, 3709–3713.
Brichau, S., Thomson, S., Ring, U., 2010. Thermochronometric constraints on the tectonic evolution of the Serifos detachment, Aegean Sea, Greece. International Journal of Earth Sciences 99, 379–393.
Buick, I.S., 1991. The late Alpine evolution of an extensional shear zone, Naxos, Greece. Journal of the Geological Society, London 148, 93–103.
Cartwright, J.A., Trudgill, B.D., Mansfield, C.S., 1995. Fault growth by segment linkage: an explanation for scatter in maximum displacement and trace length data from the Canyonlands Grabens of SE Utah. Journal of Structural Geology 17, 1319.
Clark, R.M., Cox, S.J.D., 1996. A modern regression approach to determining fault displacement-length scaling relationships. Journal of Structural Geology 18, 147–152.
Cowie, P.A., Scholz, C.H., 1992a. Displacement-length scaling relationship for faults: data synthesis and discussion. Journal of Structural Geology 14, 1149–1156.
Cowie, P.A., Scholz, C.H., 1992b. Physical explanation for the displacement-length relationship of faults using a post-yield fracture mechanics model. Journal of Structural Geology 14, 1133–1148.
Dawers, N.H., Anders, M.H., Scholz, C.H., 1993. Growth of normal faults: displacement–length scaling. Geology 21, 1107–1110.
Exner, U., Mancktelow, N.S., Grasemann, B., 2004. Progressive development of s-type flanking folds in simple shear. Journal of Structural Geology 26, 2191–2201.
Exner, U., Grasemann, B., 2010. Deformation bands in gravels: displacement gradients and heterogeneous strain. Journal of the Geological Society 167, 905–913.
Exner, U., Dabrowski, M., 2010. Monoclinic and triclinic 3D flanking structures around elliptical cracks. Journal of Structural Geology 32, 2009–2021.
Faure, M., Bonneau, M., Pons, J., 1991. Ductile deformation and syntectonic granite emplacement during the late Miocene extension of the Aegea (Greece). Bulletin de la Societe Geologique de France 5, 3–11.
Fossen, H., Hesthammer, J., 1997. Geometric analysis and scaling relations of deformation bands in porous sandstone. Journal of Structural Geology 19, 1479–1493.
Fusseis, F., Handy, M.R., Schrank, C., 2006. Networking of shear zones at the brittle-to-viscous transition (Cap de Creus, NE Spain). Journal of Structural Geology 28, 1228–1243.
Gautier, P., Brun, J.-P., Jolivet, L., 1993. Structure and kinematics of upper Cenozoic extensional detachment on Naxos and Paros (Cyclades islands, Greece). Tectonics 12, 1180–1194.
Gillespie, P.A., Walsh, J.J., Watterson, J., 1992. Limitations of dimension and displacement data from single faults and the consequences for data analysis and interpretation. Journal of Structural Geology 14, 1157–1172.
Grasemann, B., Stüwe, K., 2001. The development of flanking folds during simple shear and their use as kinematic indicators. Journal of Structural Geology 23, 715–724.
Grasemann, B., Stüwe, K., Vannay, J.-C., 2003. Sense and non-sense of shear in flanking structures. Journal of Structural Geology 25, 19–34.
Grasemann, B., Martel, S., Passchier, C., 2005. Reverse and normal drag along a fault. Journal of Structural Geology 27, 999–1010.
Grasemann, B., Petrakakis, K., 2007. Evolution of the Serifos metamorphic core complex. In: Lister, G., Forster, M., Ring, U. (Eds.), Inside the Aegean Metamorphic Core Complexes. doi:10.3809/jvirtex.2007.00170.
Guermani, A., Pennacchioni, G., 1998. Brittle precursor of plastic deformation in a granite: an example from the Mont Blanc massif (Helvetic, western Alps). Journal of Structural Geology 20, 135–148.
Gupta, A., Scholz, C.H., 1998. Utility of elastic models in predicting fault displacement fields. Journal of Geophysical Research 103, 823–834.
Iacopini, D., Passchier, C.W., Koehn, D., Carosi, R., 2007. Fabric attractors in general triclinic flow systems and their application to high strain shear zones: a dynamical system approach. Journal of Structural Geology 29, 298–317.
Iglseder, C., Grasemann, B., Schneider, D.A., Petrakakis, K., Miller, C., Klötzli, U.S., Thöni, M., Zámolyi, A., Rambousek, C., 2009. I and S-type plutonism on Serifos (W-Cyclades, Greece). Tectonophysics 473, 69–83.
Jiang, D., Williams, P.F., 1998. High strian zones: a unified model. Journal of Structural Geology 20, 1105–1120.
Jolivet, L., Brun, J.P., Gautier, P., Lallemant, S., Patriat, M., 1994. 3D-kinematics of extension in the Aegean region from the early Miocene to the present; insights from the ductile crust. Bulletin de la Societe Geologique de France 165, 195–209.
Jolivet, L., Brun, J.-P., 2010. Cenozoic geodynamic evolution of the Aegean. International Journal of Earth Sciences 99, 109–138.
Jolivet, L., Lecomte, E., Huet, B., Denèle, Y., Lacombe, O., Labrousse, L., Le Pourhiet, L., Mehl, C., 2010. The North Cycladic detachment system. Earth and Planetary Science Letters 289, 87–104.
Kim, Y.-S., Sanderson, D.J., 2005. The relationship between displacement and length of faults: a review. Earth-Science Reviews 68, 317–334.
Kocher, T., Mancktelow, N.S., 2006. Flanking structure development in anisotropic viscous rock. Journal of Structural Geology 28, 1139–1145.
Lin, S., Jiang, D., Williams, P.F., 1998. Transpression (or transtension) zones of triclinic symmetry: natural example and theoretical modelling. In: Jones, R.R., Holdsworth, R.E. (Eds.), Continental Transpressional and Transtensional Tectonics. Geological Society London Special Publication, pp. 41–57.
Lin, S., Jiang, D., 2001. Using along-strike variation in strain and kinematics to define the movement direction of curved transpressional shear zones: an example from northwestern Superior Province, Manitoba. Geology 29, 767–770.
Lister, G.S., Banga, G., Feenstra, A., 1984. Metamorphic core complexes of Cordilleran type in the Cyclades, Aegean Sea, Greece. Geology 12, 221–225.
Mancktelow, N.S., Pennacchioni, G., 2005. The control of precursor brittle fracture and fluid-rock interaction on the development of single and paired ductile shear zones. Journal of Structural Geology 27, 645–661.
Mancktelow, N.S., 2008. Interaction between brittle fracture and ductile flow during crustal deformation. Bollettino Della Società Geologica Italiana 127, 217–220.
Marrett, R., Allmendinger, R.W., 1991. Estimates of strain due to brittle faulting: sampling of fault populations. Journal of Structural Geology 13, 735–738.
McGrath, A.M., 1992. Fault propagation and growth; a study of the Triassic and Jurassic from Watchet and Kilve, North Somerset. Master Thesis, Royal Holloway, London, p. 165.
Muraoka, H., Kamata, H., 1983. Displacement distribution along minor fault traces. Journal of Structural Geology 5, 483.
Mutlu, O., Pollard, D.D., 2008. On the patterns of wing cracks along an outcrop scale flaw: a numerical modeling approach using complementarity. Journal of Geophysical Research 113. doi:10.1029/2007JB005284.
Nicol, A., Watterson, J., Walsh, J.J., Childs, C., 1996. The shapes, major axis orientations and displacement patterns of fault surfaces. Journal of Structural Geology 18, 235–248.
Passchier, C.W., 2001. Flanking structures. Journal of Structural Geology 23, 951–962.
Peacock, D.C.P., 1991. Displacements and segment linkage in strike-slip fault zones. Journal of Structural Geology 13, 1025–1035.
Peacock, D.C.P., Sanderson, D.J., 1991. Displacements, segment linkage and relay ramps in normal fault zones. Journal of Structural Geology 13, 721.
Pennacchioni, G., Mancktelow, N.S., 2007. Nucleation and initial growth of a shear zone network within compositionally and structurally heterogeneous granitoids under amphibolite facies conditions. Journal of Structural Geology 29, 1757–1780.
Pollard, D.D., Segall, P., 1987. Theoretical displacements and stresses near fractures in rocks. In: Atkinson, B.K. (Ed.), Fracture Mechanics of Rock. Academic Press, London, pp. 277–349.
Ramsay, J.G., Huber, M.I., 1983. The Techniques of Modern Structural Geology. Volume 1: Strain Analysis. Academic Press Inc. Ltd, London, 308 pp.
Ring, U., Glodny, J., Will, T., Thomson, S., 2010. The Hellenic subduction system: high-pressure metamorphism, exhumation, normal faulting, and large-scale extension. Annual Review of Earth and Planetary Sciences 38, 45–76.
Rippon, J.H., 1985. Contoured patterns of throw and hade of normal faults in the coal measures (Westphalian) of northeast Derbyshire. Proceedings of the Yorkshire Geological Society 45, 147–161.
Schlische, R.W., 1995. Geometry and origin of fault-related folds in extensional settings. AAPG Bulletin 79, 1661–1678.

Schlische, R.W., Young, S.S., Ackermann, R.V., Gupta, A., 1996. Geometry and scaling relations of a population of very small rift-related normal faults. Geology 24, 683–686.
Scholz, C.H., 2002. The mechanics of earthquakes and faulting. Cambridge University Press, New York, NY, 469 pp.
Schultz, R.A., Fossen, H., 2002. Displacement–length scaling in three dimensions: the importance of aspect ratio and application to deformation bands. Journal of Structural Geology 24, 1389–1411.
Schultz, R.A., Okubo, C.H., Wilkins, S.J., 2006. Displacement-length scaling relations for faults on the terrestrial planets. Journal of Structural Geology 28, 2182–2193.
Schultz, R.A., Soliva, R., Fossen, H., Okubo, C.H., Reeves, D.M., 2008. Dependence of displacement–length scaling relations for fractures and deformation bands on the volumetric changes across them. Journal of Structural Geology 30, 1405–1411.
Segall, P., Simpson, C., 1986. Nucleation of ductile shear zones on dilatant fractures. Geology 14, 56–59.
Soliva, R., Benedicto, A., 2005. Geometry, scaling relations and spacing of vertically restricted normal faults. Journal of Structural Geology 27, 317.
Soliva, R., Benedicto, A., Maerten, L., 2006. Spacing and linkage of confined normal faults: importance of mechanical thickness. Journal of Geophysical Research 111. doi:10.1029/2004JB003507.
Sullivan, W.A., Law, R.D., 2007. Deformation path partitioning within the transpressional White Mountain shear zone, California and Nevada. Journal of Structural Geology 29, 583–599.
Tschegg, C., Grasemann, B., 2009. Deformation and alteration of a granodiorite during low-angle normal faulting (Serifos, Greece). Lithosphere 1, 139–154.
Walsh, J.J., Watterson, J., 1988. Analysis of the relationship between displacements and dimensions of faults. Journal of Structural Geology 10, 239–247.
Walsh, J.J., Watterson, J., 1989. Displacement gradients on fault surfaces. Journal of Structural Geology 11, 307–316.
Wang, Y., Mora, P., 2008. Modeling wing crack extension: implications for the Ingredients of discrete element model. Pure and Applied Geophysics 165, 609–620.
Withjack, M.O., Schlische, R.W., Olsen, P.E., 2002. Rift-basin structure and its influence on sedimentary systems, Sedimentation in Continental Rifts. SEPM Special Publication, pp. 57–81.
Wibberley, C.A.J., Petit, J.P., Rives, T., 1999. Mechanics of high displacement gradient faulting prior to lithification. Journal of Structural Geology 21, 251–257.
Willemse, E.J.M., Pollard, D.D., Aydin, A., 1996. Three-dimensional analyses of slip distributions on normal fault arrays with consequences for fault scaling. Journal of Structural Geology 18, 295–309.